Hindawi
Shock and Vibration
Volume 2024, Article ID 4304704, 18 pages
https://doi.org/10.1155/2024/4304704

Research Article

Driving Comfort Analysis Method of Highway Bridge Based on Human-Vehicle-Bridge Interaction

Zhi-Bo Guo,[1] Jian Zou,[1] Jian-Qing Bu ,[2,3] and Ji-Ren Zhang [4]

[1]*School of Civil Engineering, Shijiazhuang Tiedao University, Shijiazhuang 050043, Hebei, China*
[2]*State Key Laboratory of Mechanical Behavior and System Safety of Traffic Engineering Structures, Shijiazhuang Tiedao University, Shijiazhuang 050043, Hebei, China*
[3]*School of Traffic and Transportation, Shijiazhuang Tiedao University, Shijiazhuang 050043, Hebei, China*
[4]*School of Civil Engineering, Hunan University, Changsha 410082, Hunan, China*

Correspondence should be addressed to Ji-Ren Zhang; jrzhang1994@hnu.edu.cn

Received 7 November 2023; Revised 16 January 2024; Accepted 17 March 2024; Published 27 March 2024

Academic Editor: Francisco Beltran-Carbajal

Research on evaluating highway bridge performance through vehicle-bridge interaction (VBI) analysis has made significant advancements. However, when assessing driving comfort, using vehicle acceleration instead of human acceleration poses challenges in accurately representing comfort. First, the paper proposes a finite element analysis method for human-vehicle-bridge spatial interactions (HVBSIs). Then, the importance of wheel path roughness difference is explored when assessing driving comfort. Furthermore, a new method for evaluating driving comfort that includes human and vehicle vibration responses has been proposed, and a simulation example of the steel-concrete composite beam bridge (SCCBB) is used to verify the effectiveness of the proposed method. The results demonstrate that the HVBSI analysis method effectively simulates the interconnected vibrations of the human body, the spatial vehicle model, and the three-dimensional (3D) bridge model. Differences in wheel path roughness significantly impact the roll vehicle vibration responses, which are crucial in driving comfort analysis. The driver's body vibration response is essential for evaluating driving comfort, and its inclusion leads to increased comfort indices values. In comparison to traditional methods, the overall vibration total value (OVTV) increases by a maximum of 109.04%, and the level of weighted vibration (L_{eq}) increases by a maximum of 6.74%. This leads to an upgrade from grade IV to grade V in terms of comfort level, indicating a reduced comfort.

1. Introduction

In recent years, there are many long-serving highway bridges subjected to adverse external factors such as weather conditions and vehicle overloading. These factors have resulted in a growing issue of road surface roughness, which significantly impairs the comfort of drivers. Therefore, assessing an individual's capacity to withstand vehicle vibrations and extending this evaluation to quantify the comfort of driving on bridges present a challenging task. The study of bridge driving comfort is closely linked to the development of VBI theory and technology. British and French scholars conducted experiments on the Britannia Bridge model in the mid-19th century to study the load-bearing capacity and dynamic performance of bridges under moving loads. In the case of highway bridges, the excitation mechanisms for VBI are more intricate. With the rapid advancement of computers and numerical simulation technology, theoretical research related to VBI has made significant strides. This includes the study of bridge dynamic impact factors, bridge fatigue issues, and bridge structural damage identification. It also involves research into vibration control on highway bridges, driving comfort on bridges, and dynamic load identification of vehicles on bridges.

To accurately evaluate the driving comfort of highway bridges, it is crucial to consider factors such as road surface roughness, bridge and vehicle dynamics, and human sensory perception. Scholars globally have conducted comprehensive experimental and theoretical studies on driving comfort, specifically addressing the coupled vibration of the vehicle-bridge system. This approach provides a more thorough understanding of driving comfort issues.

In prior studies, bridge driving comfort has often relied on assessing the driver's tolerance to vehicle vibrations [1, 2]. Some scholars have streamlined the analysis by directly using the vehicle's vibration response. This method has a high computational efficiency but a large error [3]. The processing of the vehicle's vibration acceleration results based on geometric relationships allows retroactive calculation of the driver position's vibration acceleration response. This method yields a higher calculation precision in assessing driving comfort [4]. Moreover, scholars have extensively studied the factors affecting driving comfort, with a focus on two main aspects: the impact of external adverse loads and changes in the vehicle or driving parameters on driving comfort. Research literature shows that road surface roughness and wind loads are key external factors affecting the bridge's driving comfort [5]. Furthermore, changes in parameters such as vehicle speed, weight, type, and traffic characteristics also significantly impact the bridge's driving comfort. With advancing research, there is a growing interest in investigating the intricate interactions between wind, traffic, and bridges concerning driving comfort [6]. Nguyen et al. explored safety and comfort in slender arch bridges subjected to turbulence and vehicles [7]. Research also delves into passenger comfort when vehicles traverse sea-crossing bridges in cold marine conditions with ice loads [8]. Furthermore, alterations in bridge pier height influence driving comfort to some extent [9].

Extensive research reveals the human body as a highly intricate and dynamic elastic system with vibrational characteristics influenced by environmental factors, posture, and psychological elements, displaying notable individual variations [10]. Furthermore, variations in vibrations exist between the driver and the vehicle body, a facet not adequately addressed by current driving comfort assessment standards [11]. In recent years, scholars have delved into comprehensive research on interaction analysis models for passenger-vehicle-railway bridge systems [12, 13]. For example, Wang et al. simplified passengers as a five-degree-of-freedom spring-damping model, conducting a comparative analysis of passenger and train dynamic responses [14]. They evaluated passenger comfort based on the ISO 2631 standard [15]. Similarly, Yu et al. treated passengers as a single-degree-of-freedom system attached to the bottom of the train carriages, employing the Newmark-β method to analyze the time-domain numerical solution of the passenger-train-path vertical interaction model [16]. In another study, Liu et al. developed an 8-degree-of-freedom human dynamic model and a 31-degree-of-freedom vehicle model. They explored the impact of vehicle speed, passenger count, and passenger positioning on human comfort levels [17]. These studies indicate that future research focusing on the driver's human dynamic response in the context of bridge driving comfort is meaningful.

The current research in the field of highway bridge-driving comfort primarily relies on vehicle's vibration responses. However, it often overlooks the distinctions between human and vehicle responses, which could potentially affect the evaluation of driving comfort on these bridges. This paper introduces an enhanced analysis model for the interaction within the human-vehicle-bridge system, specifically tailored to highway bridges. It also simulates road surface roughness, considering the difference in vehicle wheel paths. In addition, an evaluation method of highway-bridge driving comfort considering the vibration response of 3D space human-vehicle system and the difference in wheel path roughness is proposed. To validate this method, a three-span continuous SCCBB serves as the background. This study utilizes the proposed method for a comprehensive assessment of driving comfort for two-axle trucks and compares the results with traditional methods for evaluating driving comfort. In addition, the meanings of all abbreviations in the paper are shown in Table 1.

2. Theoretical Framework of the New Driving Comfort Evaluation Method

The new method for analyzing driving comfort on highway bridges in this paper comprises three key components. First, it introduces an interaction analysis method for the human-vehicle-bridge system. This involves creating 3D finite element models for the bridge, a spatial whole-vehicle model, and an elastic human body model to analyze the interaction relationships. Second, it considers the difference in road surface roughness between the left and right wheel paths of the vehicle during motion. The paper proposes a method to simulate this roughness in wheel paths. Lastly, it presents a comprehensive method for evaluating the driving comfort by taking into account both the human and vehicle vibration responses. In summary, this new method uses HVBSI analysis to evaluate driving comfort on highway bridges, incorporates differences in wheel path roughness, and considers both human and vehicle vibrations.

2.1. Human-Vehicle-Bridge Spatial Interaction Analysis Method. Early bridge-vehicle interaction analyses often relied on 2D planar beam models due to their computational efficiency and readily obtainable analytical solutions [18]. However, real-world bridges and vehicles exist in a 3D space, resulting in complex interaction relationships between the 3D bridge, spatial vehicles, and the human body subsystems. This complexity often leads to convergence issues in finite element analysis. To address this challenge, this section introduces an HVBSI analysis method based on ANSYS.

The method involves two computation domains: (1) for the bridge structure, solid and shell elements follow conventional meshing and (2) for the human-vehicle system, two parallel lines above the bridge deck depict its motion trajectory. This separation of the human-vehicle system mesh from the bridge structure reduces computational workload. Furthermore, updating the trajectory mesh during calculations does not require modifying the bridge structure's grid division, thus enhancing modeling efficiency.

Table 1: The meaning of abbreviations used in the paper.

Abbreviations	Meaning of abbreviation
VBI	Vehicle-bridge interaction
HVBSI	Human-vehicle-bridge spatial interactions
SCCBB	Steel-concrete composite beam bridge
3D	Three-dimensional
2D	Two-dimensional
OVTV	Overall vibration total value
L_{eq}	Level of weighted vibration
OVTV′	Overall vibration total value (obtained by the new method)
$L_{eq}^{'}$	Level of weighted vibration (obtained by the new method)
RMS	Root mean square
R0	No roughness
R1	Low-level roughness
R2	High-level roughness
R1′	Low-level roughness (consider the wheel path roughness difference)
R2′	High-level roughness (consider the wheel path roughness difference)
BVVD	Vertical vibration displacement of SCCBB
BVVA	Vertical vibration acceleration of SCCBB
VVA	Vertical vibration acceleration of vehicle
PVA	Pitch vibration acceleration of vehicle
RVA	Roll vibration acceleration of vehicle
Med1	Traditional driving comfort analysis method
Med2	New driving comfort analysis method

In addition, this method requires defining two coordinate systems: (1) reference coordinate system (R) for the initial positions of human-vehicle system trajectory nodes and (2) moving coordinate system (M) for positions at the bridge contact points during movement. Figure 1 illustrates the human-vehicle-bridge interaction method with a two-axle vehicle traveling at a constant speed on the bridge roadway. To establish the reference coordinate system at the initial analysis moment, two infinitely stiff plates are placed at both bridge ends, representing the pre-bridge and post-bridge ground. Their length is L_G, having no impact on results but accommodating the vehicle in the initial and final analysis stages.

Vectors X_R and X_M denote the positions of the human-vehicle system and bridge coupling nodes in the reference and moving coordinate systems. The following equation illustrates the use of node grid displacement functions to determine the vehicle's position on the bridge during travel:

$$\begin{gathered}\overline{\mathbf{X}} = \mathbf{X}_M - \mathbf{X}_R,\\ \mathbf{X}_R = \left[\mathrm{X}_R^1, \mathrm{X}_R^2\right]^T, \mathbf{X}_M = \left[\mathrm{X}_M^1, \mathrm{X}_M^2\right]^T,\end{gathered} \tag{1}$$

where $\overline{\mathbf{X}}$ is the vehicle's distance from the initial moment, X_R^1 and X_R^2 are the initial positions of the vehicle's front and rear wheels in the reference coordinate system, and X_M^1 and X_M^2 represent the positions of the front and rear wheels in the moving coordinate system during travel.

We define the moment when the vehicle's front wheels are about to ascend the bridge as the initial moment ($t = 0$) as

$$\mathbf{X}_R^0 = \left[0, -L_w\right]^T, \tag{2}$$

where L_w is the distance between the front and rear wheels.

Assuming that the vehicle travels at a constant speed v, then the position $\mathbf{X}_M^t$ of the vehicle in the moving coordinate system at time t is

$$\mathbf{X}_M^t = \mathbf{X}_R^0 + vt = \left[vt, -L_w + vt\right]^T. \tag{3}$$

The distance $\overline{\mathbf{X}}_t$ of the vehicle from the initial moment at any time can be determined by equations (1)–(3). This represents the constraint displacement along the vehicle's travel direction in each time step of the human-vehicle-bridge method, as shown in the following equation:

$$\overline{\mathbf{X}}_t = \mathbf{X}_M^t - \mathbf{X}_R^0. \tag{4}$$

In ANSYS, the HVBSI method involves the following steps:

(1) Establishing a 3D bridge model: the bridge model is established based on ANSYS, and the specific modeling steps can be referred from reference [18].

(2) Establishing a human-vehicle system model: An elastic human body model with three degrees of freedom is used, as shown in Figure 2. It is represented by three spring-damper elements and one mass element, corresponding to the head, upper body, legs, and body mass. The vehicle's suspension system and wheel elasticity are abstracted as elastic elements, with their energy dissipation represented by dampers. The vehicle is abstracted as a rigid body with its mass assumed to be concentrated at the center of this rigid body. The vehicle model accounts for vertical, pitch, and roll degrees of freedom in the vehicle body, along with vertical wheel movement. The stiffness factors, damping factors, and mass for each part of the human-vehicle model are assigned through the R command.

(3) Applying constraints to the human-vehicle model nodes: to ensure effective vibration transmission between the vehicle and the human body, vertical

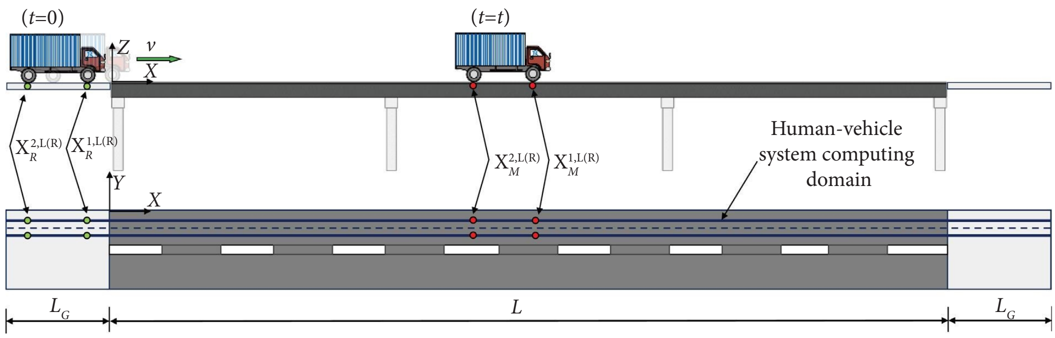

FIGURE 1: Human-vehicle-bridge interaction analysis method.

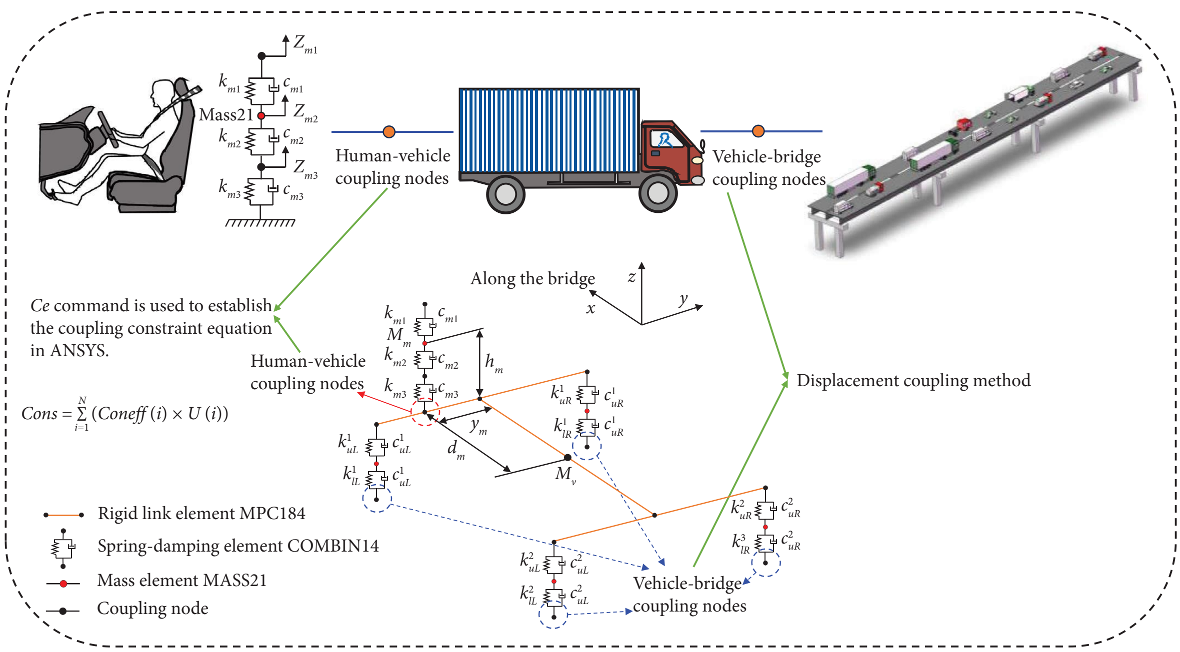

FIGURE 2: Human-vehicle-bridge space coupling nodes.

contact (Uz) between the vehicle and the human is established through the *Ce* command. This implementation follows a coupling constraint equation as per equation (5). In this equation, *Cons* is set to 0, *N* is set to 2, *Coneff* (1) is set to 1, and *Coneff* (2) is set to −1. Other contact directions are constrained by using the *D* command, thus securing their degrees of freedom. Vertical contact between the vehicle body and the suspension's top nodes is handled in the same manner. The vehicle mass point, M_v, is constrained in the Ux, Uy, and Rotz directions while releasing other degrees of freedom. At the wheel nodes and other unspecified vehicle rigid body nodes, Uz direction degrees of freedom are released, while other directions are constrained.

$$\text{Cons} = \sum_{i=1}^{N} \left(\text{Cone}ff\,(i) \times U\,(i)\right), \tag{5}$$

where *Cons* represents the constant term within the constraint equation, *Coneff* (i) denotes the coefficient for the i-th node, U (i) signifies the i-th degree of freedom, and N stands for the total number of terms in the equation.

(4) Achieving the HVBSI analysis. To achieve the HVBSI analysis, we applied different horizontal constraint displacements (Ux) of magnitude $\overline{\mathbf{X}}_t = \mathbf{X}_M^t - \mathbf{X}_R^0$ to the four vehicle-bridge coupling nodes in each load step (implemented via the *D* command based on known velocities). At the end of each load step, the constraints were reapplied to the human-vehicle system nodes as outlined in step (3). We coupled the four-axle nodes with the nodes moved to the bridge surface using vertical displacement (Uz) as per equation (5). We considered bridge surface roughness with samples defined by the *Cons* parameter in equation (5). Then, we used a **do* loop

command to iterate through all load steps until $\overline{\mathbf{X}}_t = [L + L_w, L]$, indicating the completion of calculations as the vehicle leaves the bridge.

2.2. A Simulation Method considering the Roughness Difference of Wheel Paths. Road surface roughness plays a crucial role in affecting vehicle vibration response. While past studies extensively explored simulating roughness along the longitudinal axis of the bridge, coupling a spatial vehicle model with bridge analysis reveals noticeable differences in roughness along the transverse wheel paths.

In Figure 3, roughness differs between paths I and II, affecting the five wheels on path I simultaneously. In addition, at a specific moment, wheel 3's roughness consistently matches those experienced by wheel 2 T_w seconds earlier, with time gaps between roughness for each adjacent pair of wheels. Using 2D rod or beam elements in the bridge model overlooks these roughness differences, potentially impacting coupled vehicle-bridge dynamic response results. Introducing an elastic human model in the vehicle for a human-vehicle-bridge interaction analysis may further amplify this impact, often neglected in prior research.

The road surface roughness is treated as a zero-mean Gaussian random process, and the power spectral density of the road surface roughness can be expressed as follows:

$$G_d(n) = G_d(n_0)\left(\frac{n}{n_0}\right)^{-w}, \quad (6)$$

where $G_d\ (n_0)$ represents the bridge surface roughness coefficient, determined based on the bridge surface roughness levels defined in the "Vehicle vibration-Describing method for road surface roughness" GB/T7031-2005 [19]. Different road surface roughness levels (R0, R1, and R2) are defined by using the parameter $G_d(n_0)$. The parameter n_0 signifies the reference spatial frequency, typically set to $0.1\,\mathrm{m}^{-1}$. The frequency exponent, denoted as w, is commonly assigned a value of 2, and n represents the spatial frequency (m^{-1}). The samples of bridge surface roughness values are generated by using the triangular series method, as shown in the following equation:

$$r(x) = \sum_{k=1}^{N}\left(4G_d(n_0)\left(\frac{2\pi k}{L_c n_0}\right)^{-2}\frac{2\pi}{L_c}\right)^{0.5}\cos\left(\frac{2\pi k n_0}{L_c} + \theta_k\right), \quad (7)$$

where $r(x)$ represents the bridge surface roughness value at a specific node along the bridge surface, with x denoting the distance from the starting point of the bridge, N represents the number of sampling points, L_c is the length of the bridge surface considered for roughness, and θ_k represents a set of independent random variables following a uniform distribution in the range of $[0, 2\pi]$. The meanings of other parameters are consistent with those in equation (6).

The method for simulating road surface roughness while considering differences in wheel paths is implemented based on the HVBSI method and involves the following steps:

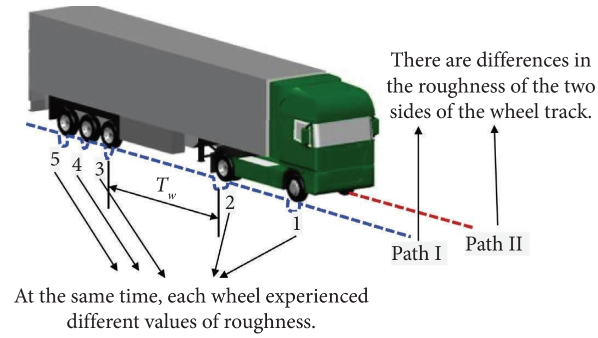

Figure 3: Vehicle wheel paths' roughness difference.

(1) Using the power spectral density of road surface roughness and the trigonometric series method stochastically, we generated two sets of roughness samples. The length of these samples should match the number of finite element nodes along the bridge surface corresponding to the vehicle's path.

(2) Then, the roughness sample values were stored as TXT files in the ANSYS working directory.

(3) The time required for an element length (T_n) was determined by the ratio of the longitudinal distance between every two bridge nodes (L_n) to the vehicle speed (v), as shown in equations (8) and (9). This, in turn, established the wheelbase time gap (T_w) based on the distance between adjacent vehicle axles.

$$T_n = \frac{L_n}{v}, \quad (8)$$

$$T_w^{i,i+1} = \left(\frac{L_w^{i,i+1}}{L_n}\right)\cdot T_n, \quad (9)$$

where i denotes the axle number. For example, for a two-axle vehicle, i equals 2, and so forth.

(4) We then used the **Create* and **Vread* commands to access the two sets of roughness data, as shown in equation (10). At the end of each time step, the roughness sample values were determined for each wheel at the next moment T based on the wheelbase time gap. Finally, these roughness values were substituted into the coupling constraint equations at points where the vehicle's wheels connected with the bridge surface (refer to step 4 in the previous section).

$$\mathbf{R}_L = \left[x_L^1, x_L^2, \cdots, x_L^n\right]^T \mathbf{R}_R = \left[x_R^1, x_R^2, \cdots, x_R^n\right]^T, \quad (10)$$

$$R_{L(R)}^i = \left(\frac{T}{T_n}\right) + \left(T_w^{i-1,i}\right)^{i-1}, \quad (11)$$

$$r_L^i(T) = x_L^{R_L^i}\ r_R^i(T) = x_R^{R_R^i}, \quad (12)$$

where R_L and R_R are the roughness samples for the left and right sides of the vehicle's paths. T represents a specific moment during the vehicle's travel. $\mathbf{R}^i_{L(R)}$ is the index of roughness samples for each wheel at time T, where L and R indicate the left and right sides of the vehicle, and i is the axle number. $r^i_L(T)$ represents the roughness value for the i-th wheel on the left side of the vehicle at time T.

(5) Finally, HVBSI analysis was performed till all time steps were completed. Then, we moved to the POST26 postprocessing module to extract dynamic response results, considering the differences in path roughness.

2.3. New Method for Evaluating Driving Comfort. In this section, a method for assessing the driving comfort of vehicle drivers is proposed, considering the dynamic response of the backrest, seat, vehicle floor, and the driver body's center of mass. This method differs from traditional driving comfort evaluations by considering both the driver and vehicle vibrations and accounting for the roughness difference of wheel paths. The traditional method only focuses on vehicle vibration and does not address the roughness difference of wheel paths.

The ISO 2631 standard specifies that 12 vibration components sufficiently represent the vibration exposure for a seated driver, as illustrated in Figure 4. Previous studies have indicated that the impact of vibration in the vehicle's longitudinal, lateral, and yawn directions on human comfort can generally be neglected [20–22]. Therefore, when transferred to the driver, only five directions of vibrations are typically considered: vertical vibration of the vehicle floor (z_f), vertical vibration of the backrest (z_b), vertical vibration (z_s), pitch vibration (r_y), and roll vibration (r_x) for the seat. These five types of vibration are fundamentally derived from vehicle vibration accelerations (see equations (13a)–(13c)).

To account for the differences between human and vehicle vibration responses, this method considers vertical vibration at the driver body's center of mass (z_h) in addition to the five vibrations associated with the vehicle. The vertical vibration response of the human body can be extracted directly by using the HVBSI method.

$$a_{zs} = a_{zb} = a_{zf} = \ddot{Z}_v, \tag{13a}$$

$$a_{ry} = \ddot{\theta}_v \cdot d_s, \tag{13b}$$

$$a_{rx} = \ddot{\varphi}_v y_s + 0.5\ddot{\varphi}_v h_s, \tag{13c}$$

where a_{ij} is the acceleration time histories in various directions for the driver, where i and j have the meanings as explained in the first paragraph of this section. Furthermore, a_z, r_y, and r_x denote the vertical, pitch, and roll vibration accelerations of the vehicle's center of mass. d_s, y_s, and h_s, respectively, denote the longitudinal, lateral, and vertical distances between the vehicle's center of mass and the seat.

Considering the variations in a driver's sensitivity to vibration direction and frequency, the ISO 2631 standard introduces frequency weighting functions for different vibration directions. These weighting functions adjust the vibration acceleration for various directions to simulate the impact of vibrations at different frequencies on driver comfort (see Figure 4). Given that, a driver primarily experiences vertical vibrations through direct contact with the seat support surface during vehicle operation. This method assumes that the frequency weighting function for vertical vibration at the driver body's center of mass (z_h) is calculated based on W_k.

The frequency-weighted acceleration in all directions is calculated by using the fast Fourier transform (FFT) method. Initially, there is a time-varying acceleration time-history signal, denoted as $a(t)$. It undergoes discrete Fourier transform (DFT) to convert the time-domain acceleration time-history signal $a(t)$ into the frequency domain (consisting of N discrete values, $a(t) = a(i)$, where $i = 1, 2, 3, \ldots, N$). This transformation reveals the distribution of the original acceleration time-history signal $a(t)$ at various frequencies, as shown in the following equation:

$$A(r) = \sum_{k=0}^{N-1} a(k)\left(e^{-2\pi r/N}\right)^{rk}, \quad r = (0, 1, \ldots, N-1). \tag{14}$$

After DFT transformation, $A(r)$ becomes a set of complex conjugate numbers. Frequency weighting is applied to $N/2$ data points in $A(r)$ containing relevant information. This involves multiplying $A(r)$ by the frequency weighting function $W(r)$ for both real and imaginary parts, thus resulting in the frequency-weighted acceleration frequency domain data $A'(r)$, as shown in equation (15). Finally, DFT converts $A'(r)$ back into the time-domain acceleration signal $a'(t)$, as shown in the following equation:

$$A'(r) = A(r) \cdot W(r), \tag{15}$$

$$a'(j) = \frac{1}{N} \sum_{r=0}^{N-1} A'(r)\left(e^{-2\pi r/N}\right)^{-jr}, \quad j = (0, 1, \ldots, N-1). \tag{16}$$

The calculation of comfort levels relies on the method of HVBSI analysis, which involves the following five main steps:

(1) The HVBSI method is employed to compute the vibration acceleration in different directions at the vehicle's center of mass, as well as the VVA of the driver's body. In this process, the influence of the roughness difference of the wheel path is considered. Following this, the vibration accelerations of the vehicle's seats, backrest, and floor are derived by using equation (13).

(2) Using FFT analysis, each vibration acceleration time history $a_{ij}(t)$ is frequency-weighted, resulting in time-domain vibration acceleration data $a'_{ij}(t)$ for the driver's body, seat, backrest, and floor.

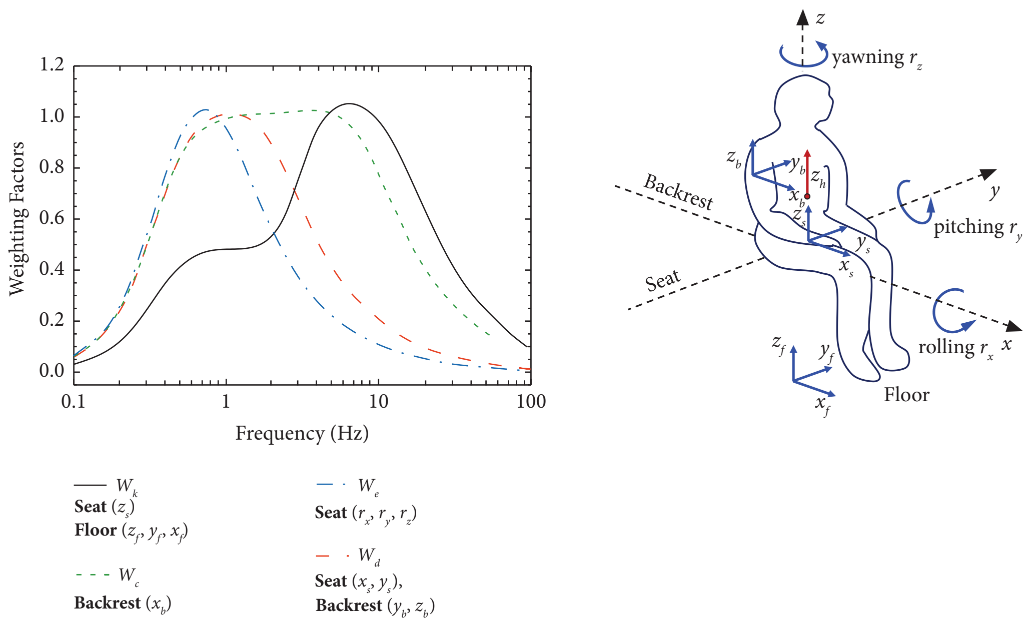

Figure 4: Frequency weighting function and the driver seated coordinate system.

(3) We then perform the calculation of root mean square (RMS) values for the vibration acceleration time histories after frequency weighting as

$$\mathrm{RMS}_{ij} = \left\{ \frac{1}{T} \int_0^T \left[a'_{ij}(t) \right]^2 dt \right\}^{1/2}, \tag{17}$$

where T is the total duration of the vibration acceleration time path $a'_{ij}(t)$.

(4) The ISO 2631 standard specifies axis weighting factors for vibrations in various directions, as shown in Table 2. By applying axis weighting factors, the RMS_{ij} values of various types of vibration accelerations are weighted and summed to obtain the OVTV, as shown in equation (18). We then calculate the L_{eq} based on the OVTV, as shown in the following equation:

$$\mathrm{OVTV} = \left\{ \sum \left(K_{ij} \mathrm{RMS}_{ij} \right)^2 \right\}^{1/2}, \tag{18}$$

$$L_{eq} = 20 \lg \left(\frac{\mathrm{OVTV}}{a_0} \right), \tag{19}$$

where the meaning of the subscript i and j is the same as that of the equation (13). K_{ij} denotes the axis weighting factors and a_0 is the RMS value of the reference acceleration, that is, $a_0 = 10^{-6}\,\mathrm{m/s^2}$.

Noteworthily, ISO 2631 does not provide clear guidelines for axis weighting factors in vertical vibrations at the driver's body's center of mass. Consequently, the author approaches the determination of these factors from two perspectives: (1) assuming that both the seat and the driver's body's vertical vibration responses consistently contribute to the overall human-vehicle system dynamics in theory and (2) in the human-vehicle system, the driver's body's vertical vibration response is caused by the vehicle seat's vertical vibration. There is a transmission relationship between them. Based on the analysis, the paper aligns the axis weighting factors for vertical vibrations at the driver's body's center of mass with those of the seat, as shown in Table 2.

(5) ISO 2631 standard classifies comfort levels based on the relationship between human subjective feelings and the OVTV. It also considers the L_{eq}. These classifications are detailed in Table 3, and the relevant parameters are derived from experiments on human vibration comfort [23].

The technical route of the new driving comfort analysis method is shown in Figure 5.

3. Case Analysis

3.1. Bridge Profile. This study focuses on a three-span continuous SCCBB. The bridge has a span of 3×40 meters and a width of 12.75 meters. It is designed for highway class I loading, with a single lane in each direction and a design speed of 100 km/h. Structural parameters can be found in [24]. The finite element model is built using ANSYS APDL commands, with reference to the element types illustrated in Figure 6. The bridge model includes a total of 90,920 nodes and 66,610 elements.

3.2. Human-Vehicle System. Studies show that vehicle weight significantly influences driving comfort, with lighter vehicles leading to higher RMS values of weighted vibration acceleration and increased discomfort. To account for the most unfavorable impact while managing the complexity

Table 2: Axis weighting factors of vibration component.

Factors	Value	Position	Direction
K_{zs}/K_{zh}	1.00	Seat/human	Vertical
K_{ry}	0.40	Seat	Pitch
K_{rx}	0.20	Seat	Roll
K_{zb}	0.40	Back	Vertical
K_{zf}	0.40	Floor	Vertical

Table 3: Comfort evaluation criteria based on OVTV and L_{eq}.

OVTV (m/s^2)	L_{eq} (dB)	Comfort level	Comfort grade
<0.315	<110	Not uncomfortable	I
0.315~0.630	110~116	Slightly uncomfortable	II
0.500~1.000	114~120	Fairly uncomfortable	III
0.800~1.600	118~124	Uncomfortable	IV
1.250~2.500	122~128	Very uncomfortable	V
>2.000	126	Extremely uncomfortable	VI

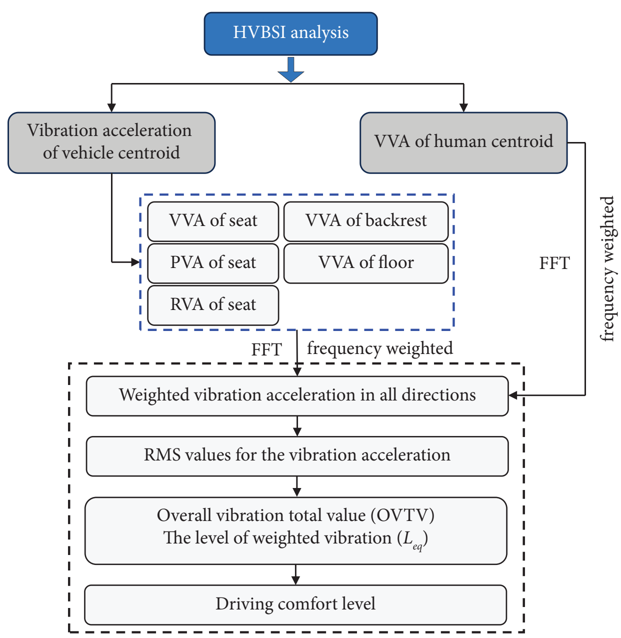

Figure 5: Technical route for HVBSI analysis.

introduced by incorporating a human model into the system, a lightweight two-axle truck is chosen for the study (see Table 4 for vehicle and human parameter values). The finite element model of the human-vehicle system has been detailed in the first section of the paper. It will not be reiterated here.

3.3. Scenario Setting. The study in this paper focuses on the following key areas: (1) assessing the effectiveness of the HVBSI analysis method, (2) highlighting the necessity of simulating road surface roughness considering wheel path differences, and (3) comparing the newly proposed method for evaluating driving comfort in this paper with the traditional comfort evaluation methods. The specific scenarios are as follows:

(1) For the first key area, two scenarios are considered: single-vehicle crossing and human-vehicle system crossing (without considering the wheel path roughness differences). Each scenario is tested at four different speeds: 40 km/h, 60 km/h, 80 km/h, and 100 km/h.

(2) For the second key area, two scenarios are considered: human-vehicle system crossing with wheel path roughness differences and human-vehicle system crossing without wheel path roughness differences. Each scenario is tested at four different speeds: 40 km/h, 60 km/h, 80 km/h, and 100 km/h. Three levels of road surface roughness are also taken into account: no roughness (R0), low-level roughness (R1), and high-level roughness (R2). R1′ and R2′

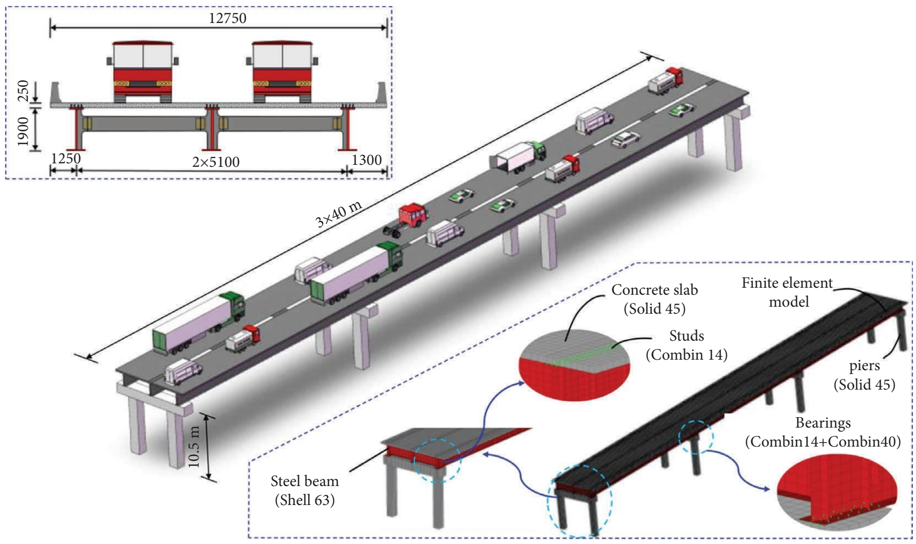

Figure 6: Finite element model of SCCBB.

Table 4: Mechanical parameters of the human-vehicle system.

Parameters	Value
I_{yz} (kg·m^2)	2950
I_{zx} (kg·m^2)	34000
k_{uL}^{i} (10^3 kN/m)	0.20/0.23
k_{uR}^{i} (10^3 kN/m)	0.20/0.23
k_{lL}^{i} (10^3 kN/m)	0.36/0.42
k_{lR}^{i} (10^3 kN/m)	0.36/0.42
c_{uL}^{j} (kN·s·m^{-1})	3.85/2.72
c_{uR}^{j} (kN·s·m^{-1})	3.85/2.72
c_{lL}^{j} (kN·s·m^{-1})	3/3
c_{lR}^{j} (kN·s·m^{-1})	3/3
M_{yz} (t)	13
M_{aa} (t)	0.8/0.7
k_{mq} (N/m)	52600/53477/39163
c_{mq} (N·s·m^{-1})	3580/3580/2384
M_m (kg)	60

denote the consideration of wheel path roughness differences, while R1 and R2 denote the absence of such differences.

(3) For the third key area, two analysis methods are considered: the newly proposed method for evaluating driving comfort and the traditional driving comfort evaluation methods. Both methods are applied to human-vehicle system crossing scenarios considering wheel path roughness differences. Each method is tested at four different speeds and three levels of road surface roughness, which is consistent with the scenarios in the second key area.

The technical route is depicted in Figure 7. Previous research has shown that vehicle weight is one of the significant factors affecting vehicle comfort. Smaller vehicle weight leads to higher RMS values of weighted vibration acceleration and greater discomfort [3]. To consider the most adverse effects, this study focuses on a lightweight two-axle truck as the research subject. Specific details and parameters of this vehicle can be found in reference [4].

3.4. Verification of the HVBSI Analytical Method. VBI analysis with finite element methods is well-established. However, when incorporating an elastic human body model into a spatial vehicle model, it is crucial to confirm the functionality of the HVBSI analysis program. This involves verifying result convergence and alignment with typical expectations.

Prior studies show that BVVD time curves at the midpoint of midspan often display a U-shaped pattern in traditional VBI analysis. Practically, if vehicle type, speed, and road roughness remain consistent, the vibration response in the midpoint of the bridge's span should be almost the same for both a single-vehicle model and a human-vehicle model crossing it. Based on the abovementioned analysis, the following section conducts a study using the scenarios set in the first key area (refer to the previous section).

By observing Figure 8, it becomes clear that the trends in the BVVD time-history curves obtained through HVBSI and VBI methods closely align and demonstrate good agreement. However, the BVVA values obtained using the HVBSI method are marginally higher than those obtained from the VBI method, and this variance can be attributed to the transmission characteristics of the elastic human body model. Nevertheless, when viewed from a broader perspective, the trends in the midpoint BVVA time-history curves from both methods consistently agree.

To avoid relying solely on a single speed calculation result, additional analysis was carried out for scenarios involving speeds of 60 km/h, 80 km/h, and 100 km/h. Figures 9(a) and 9(b) illustrate the peak of BVVD and the RMS of BVVA, calculated using both the HVBSI and VBI

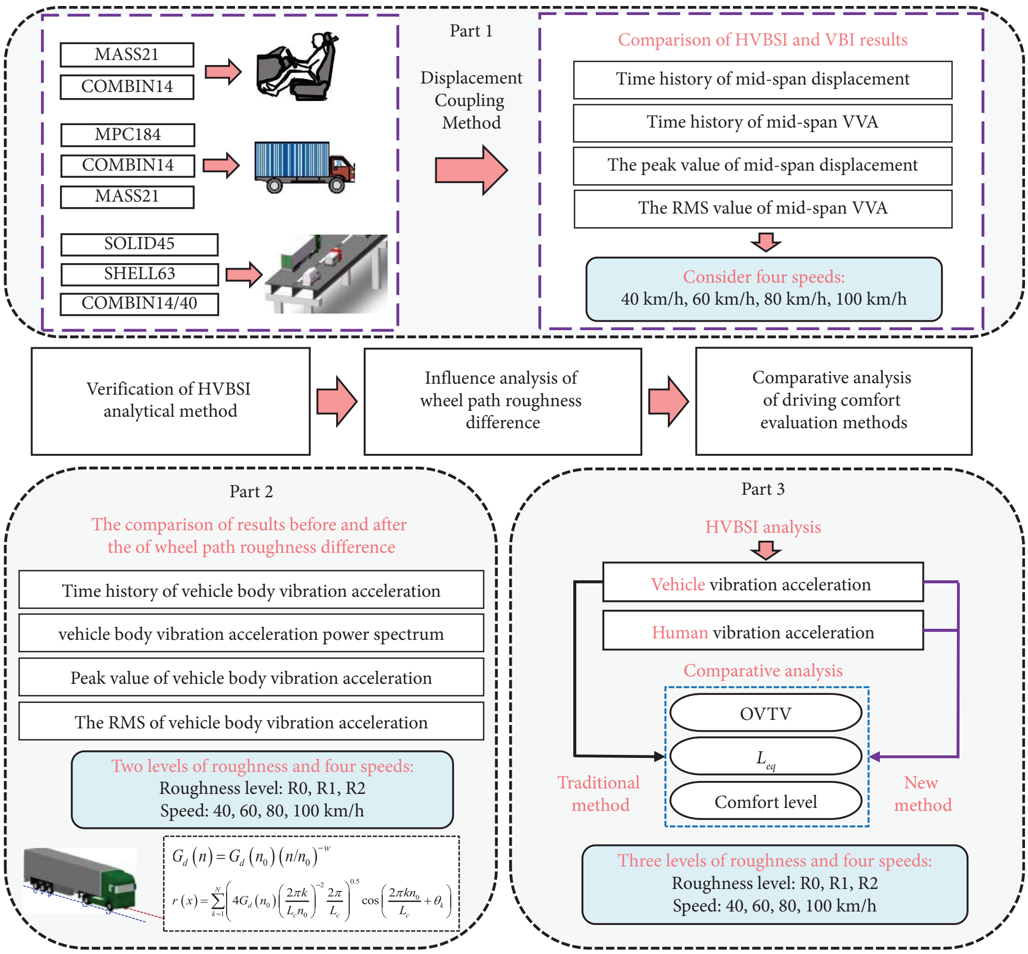

FIGURE 7: Technical route.

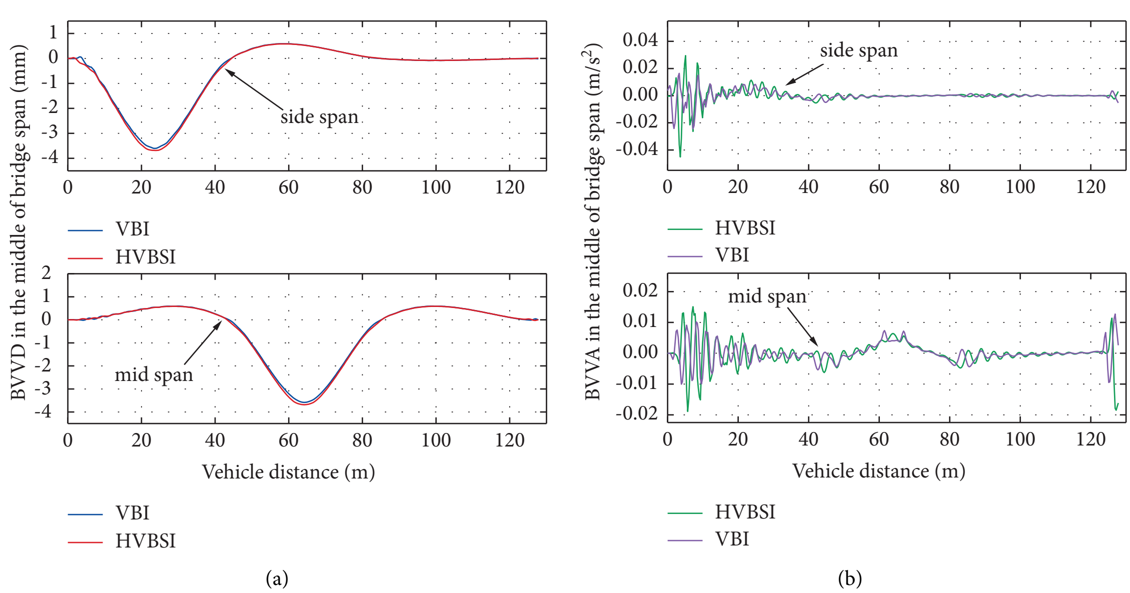

FIGURE 8: Comparison of vertical vibration response in the midpoint of side (mid) span. (a) Vertical vibration displacement. (b) Vertical vibration acceleration.

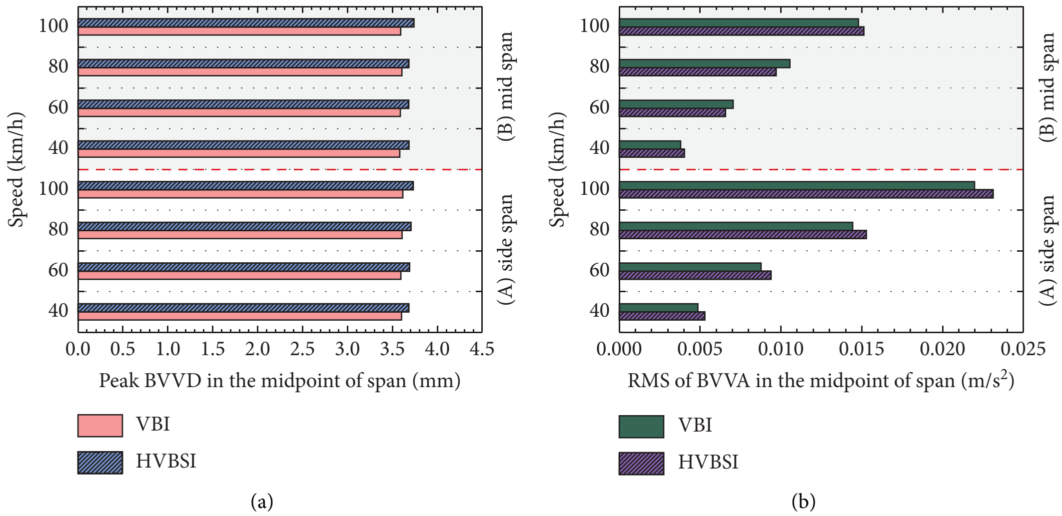

Figure 9: Comparison of vertical vibration response in the midpoint of side (mid) span of HVBSI and VBI. (a) The peak of vertical vibration displacement. (b) The RMS of vertical vibration acceleration.

methods across various speed scenarios. Figure 9 clearly shows that, when the speed is consistent, the peak BVVD values obtained using both methods are almost identical. In addition, the differences in the RMS of BVVA are minimal. Furthermore, Table 5 provides the relative errors in peak BVVD and RMS of BVVA obtained through the HVBSI and VBI methods. For each speed scenario, the relative error in peak BVVD calculated by both methods is under 4%, while the relative error in the RMS of BVVA is less than 9%.

Thus, by integrating an elastic human body model into the VBI method, the HVBSI calculation program performs effectively. Furthermore, the vertical vibration response results of the bridge, obtained through both HVBSI and VBI methods, demonstrate a high degree of agreement. This confirms the viability of the HVBSI method presented in this paper and supports its suitability for future analyses.

3.5. Influence Analysis of Wheel Path Roughness Difference. At 40 km/h, Figure 10 illustrates vehicle vibration acceleration time histories, comparing scenarios with and without wheel path roughness differences. In Figure 10(a), VVA and PVA time-history curves show similar trends and close acceleration amplitudes under R1 roughness, regardless of these differences. However, considering wheel path roughness differences results in a notable change in the RVA time history, displaying a significant increase in amplitude compared to the scenario without these differences. Similar observations apply to R2 roughness, as depicted in Figure 10(b).

In Figure 11, the VVA peaks and PVA peaks of the vehicle show no significant variation under different speeds, regardless of wheel path roughness differences. However, when considering these differences, RVA peaks experience a substantial increase. In addition, the consideration of wheel path roughness differences results in a maximum percentage change of 23.2% in VVA peaks and 20.6% in PVA peaks, as indicated in Table 5.

From Table 6 and Figure 11(c), it is evident that with constant road roughness and vehicle speed, the increase in RVA, when considering path roughness difference, far surpasses PVA and VVA. This effect is more pronounced with road roughness R2 compared to R1. Poorer road conditions amplify the impact of considering path roughness differences on RVA. At a speed of 100 km/h and road roughness R2, RVA exhibits the maximum increase at 12583.0%, while corresponding increases for VVA and PVA are only 2.8% and 11.4%, respectively. This phenomenon highlights the substantial impact of wheel path roughness differences on the vehicle's roll vibration.

Figure 12 illustrates that considering wheel track unevenness differences leads to increased RMS values for VVA, PVA, and RVA. Notably, VVA and PVA experience modest maximum increases of 17.24% and 21.96%, respectively. Conversely, RVA is significantly impacted by wheel track unevenness differences, with a staggering maximum increase of 22,839.22%. Upon further calculation of OVTV and L_{eq} values, it becomes evident that, with constant road roughness class and speed, OVTV values considering wheel track unevenness differences surpass those without such considerations. Similarly, L_{eq} values exhibit a comparable pattern, as shown in Figure 13.

Thus, considering wheel path roughness differences results in slightly increased vertical and pitch vibration responses of the vehicle, but the impact is relatively small. However, it significantly affects roll vibration response.

3.6. Comparative Analysis of Driving Comfort Evaluation Methods. Traditional methods for assessing driving comfort primarily rely on evaluating vehicle's vibration responses to

Table 5: Comparison of bridge vibration response relative error.

Position	Side span				Midspan			
Speed (km/h)	40	60	80	100	40	60	80	100
Peak BVVD	2.18%	2.64%	2.67%	3.11%	2.75%	2.52%	2.10%	3.93%
RMS of BVVA	8.85%	6.97%	5.85%	5.23%	6.07%	6.68%	8.14%%	2.21%

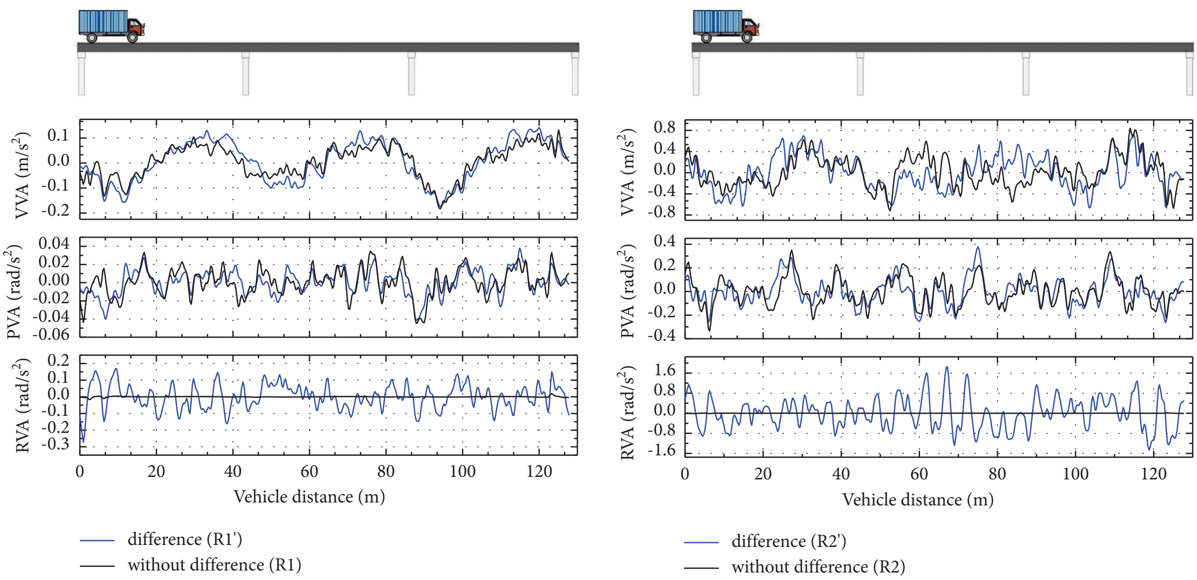

Figure 10: The time-history curve of vehicle body's vibration acceleration without the wheel path roughness difference. (a) R1-level road surface roughness. (b) R2-level road surface roughness.

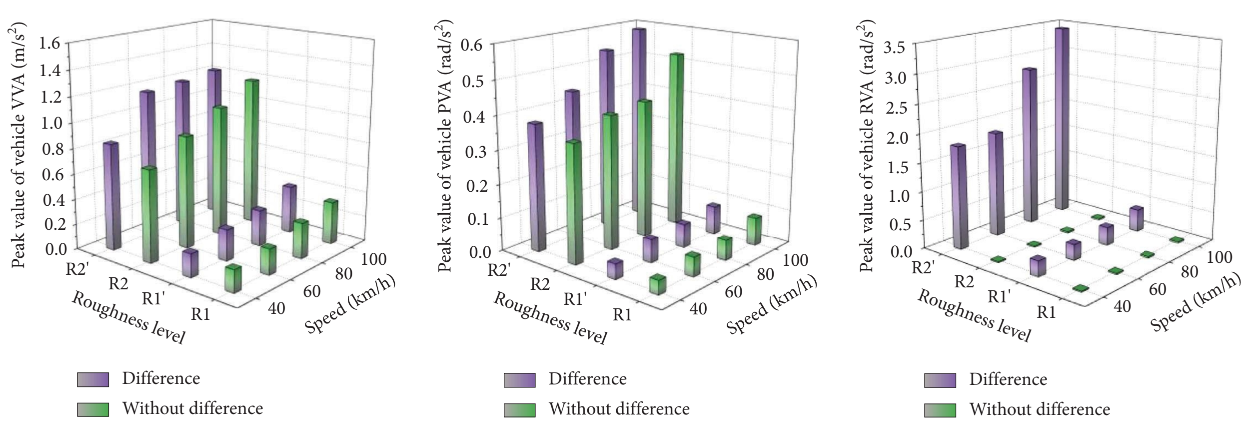

Figure 11: The peak value of vehicle's vibration acceleration without the wheel path roughness difference. (a) The peak value of VVA. (b) The peak value of PVA. (c) The peak value of RVA.

judge a driver's comfort, as outlined in reference [22]. The previous section of the paper demonstrates the significant impact of considering wheel path roughness differences on vehicle RVA. To account for this influence, all subsequent driving comfort analyses consider wheel path roughness differences.

We compared and analyzed OVTV and L_{eq} values obtained from both the traditional and new methods, as shown in Figures 14 and 15. OVTV$'$ and L_{eq}' represent the results obtained by using the new method. From Figure 14, it is evident that, regardless of the road surface roughness level, both the traditional and new methods yield

Table 6: The percentage change of peak acceleration of vehicle's vibration without the wheel path roughness difference.

Speed (km/h)	Roughness level	VVA (%)	PVA (%)	RVA (%)
40	R1	5.6	8.5	1311.4
	R2	16.0	7.9	9178.4
60	R1	23.2	20.6	1187.5
	R2	31.4	11.3	8402.3
80	R1	1.7	19.1	1172.0
	R2	14.6	32.0	11180.0
100	R1	11.7	0.2	1400.0
	R2	2.8	11.4	12583.0

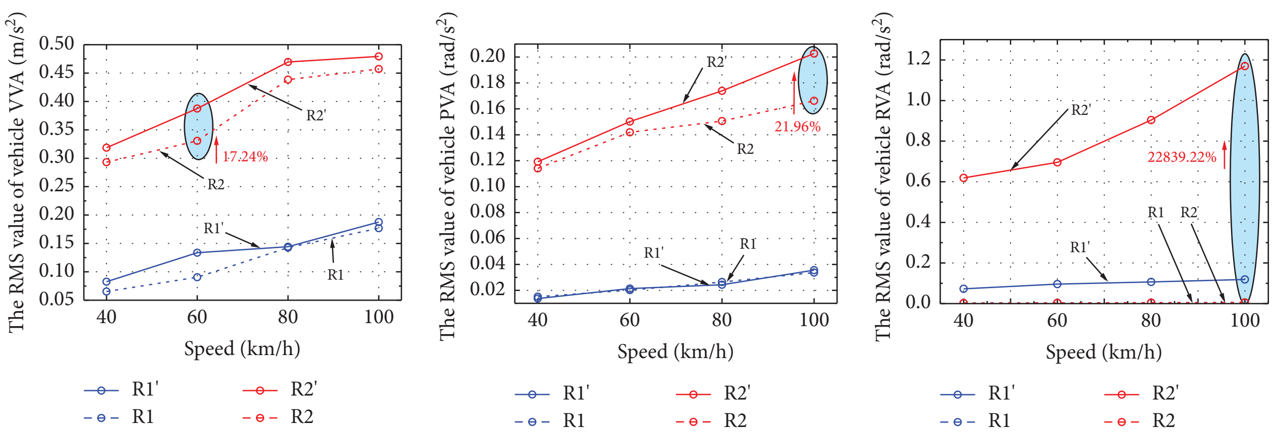

(a) (b) (c)

Figure 12: The RMS value of the vehicle body's vibration acceleration changes. (a) The RMS value of vehicle VVA. (b) The RMS value of vehicle PVA. (c) The RMS value of vehicle RVA.

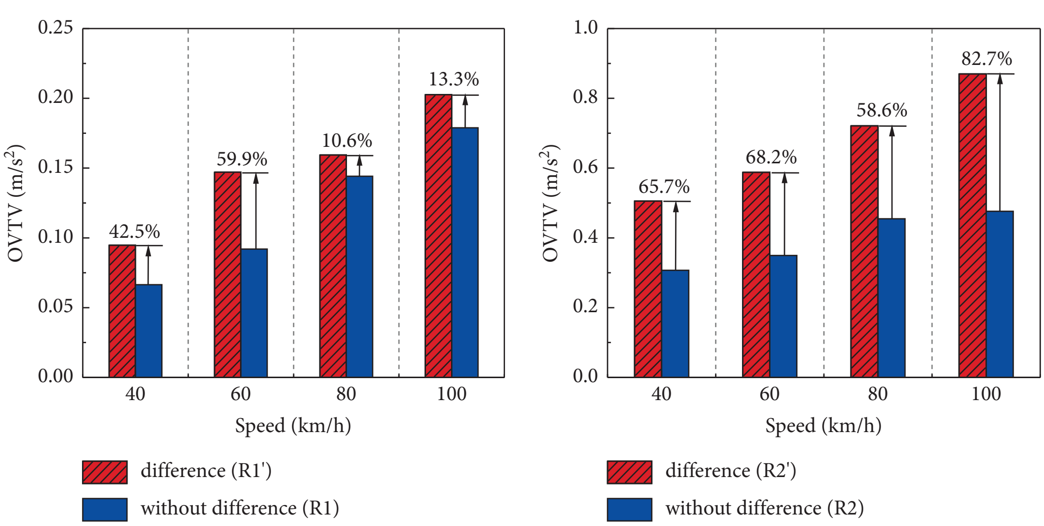

(a) (b)

Figure 13: Continued.

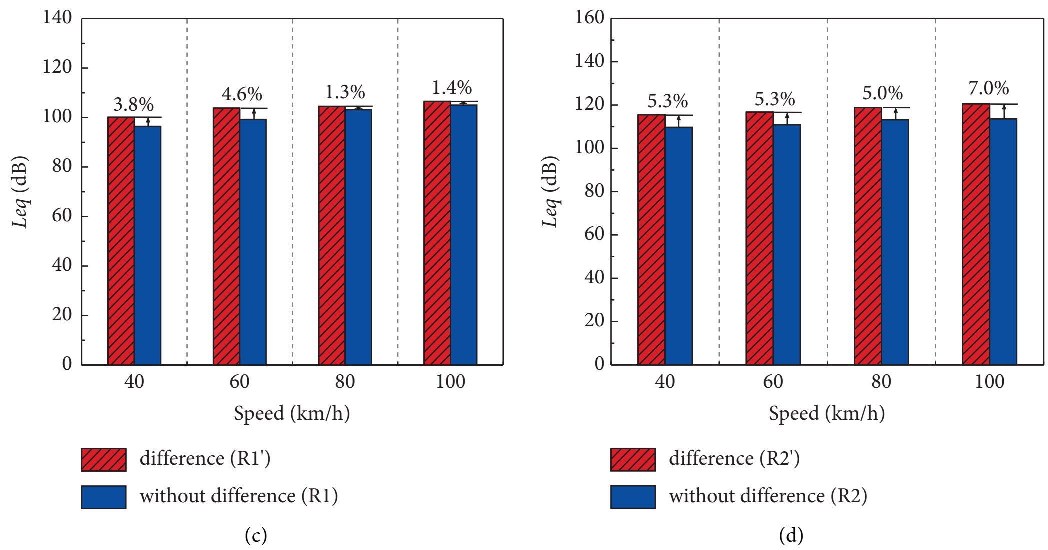

FIGURE 13: The variation of OVTV (L_{eq}) value considering the wheel path roughness difference. (a) The OVTV value of R1 roughness. (b) The OVTV value of R2 roughness. (c) The L_{eq} value of R1 roughness. (d) The L_{eq} value of R2 roughness.

increasing OVTV values with higher vehicle speeds. Notably, OVTV′ values obtained using the new method consistently exceed those obtained using the traditional method. A similar pattern is observed in the results of L_{eq} values. For Table 7, it is observed that for a road surface roughness level of R0, the new method yields OVTV′ values ($L_{eq}^{'}$ values) with a maximum increase of 109.04% (6.74%) compared to the OVTV values (L_{eq} values) obtained through the traditional method. For a road surface roughness level of R1, the maximum increases are 104.32% and 5.97%, respectively. Under R2 surface roughness conditions, these maximum increases are 91.04% and 4.87%, respectively. The maximum values of these increases are shown in bold in Table 7.

Figure 15 shows that at a constant vehicle speed, both methods produce higher OVTV and L_{eq} values as the road surface roughness level increases. Similarly, with constant vehicle speed and road surface roughness level, the OVTV′ and $L_{eq}^{'}$ values obtained using the new method consistently surpass the results obtained through the traditional method (OVTV and L_{eq}). The impact of road surface roughness on comfort indices is outlined in Table 8. Table 8 demonstrates that at a speed of 40 km/h, under the influence of three different road surface roughness levels, the maximum increase in OVTV′ values relative to OVTV values is 108.40%. Likewise, the maximum increase for $L_{eq}^{'}$ values relative to L_{eq} values is 6.74%. When the vehicle speeds are 60 km/h, 80 km/h, and 100 km/h, the maximum increases for OVTV′ values relative to OVTV values are 108.79%, 108.84%, and 109.04%, respectively. In addition, for $L_{eq}^{'}$ values relative to L_{eq} values, the maximum increases are 6.54%, 6.40%, and 6.31%, respectively. The maximum values of these increases are shown in bold in Table 8.

Based on both the traditional method (Med1) and the new method (Med2), further analysis was conducted to determine the driving comfort grades under three road surface roughness levels and four vehicle speeds, as shown in Figure 16. Figure 16 reveals that, when not considering road surface roughness (R0), both the traditional and new methods yield a driving comfort level of grade I (not uncomfortable). However, for road surface roughness level R1, at vehicle speeds of 40 km/h and 60 km/h, both methods produce identical grade I (not uncomfortable) driving comfort levels. As the vehicle speed increases to 80 km/h and 100 km/h, the new method results in grade II (slightly uncomfortable), while the traditional method maintains grade I (not uncomfortable) driving comfort levels.

The modified content is as follows: When the road surface roughness level is R2 and is calculated using the traditional method, the resulting driving comfort levels for four different vehicle speeds are grade III, grade III, grade III, and grade IV, respectively. Conversely, the new method calculates higher driving comfort levels, specifically grade IV, grade IV, grade V, and grade V for the respective vehicle speeds. In particular, a higher grade indicates a lower level of comfort.

Thus, when analyzing driving comfort using the newly proposed method (which includes the driver's body's vibration response), OVTV and L_{eq} show an increase compared to the traditional methods that solely consider vehicle vibration response. When speed and road surface roughness levels remain constant, the driving comfort levels obtained using the new method are consistently equal to or greater than those obtained through the traditional method. This suggests that the traditional method tends to be conservative in assessing driving comfort. Taking the driver's body's vibration response into account results in a deterioration of driving comfort. This illustrates the necessity of considering both the driver's vibration response and the vehicle's vibration response when evaluating ride comfort comprehensively.

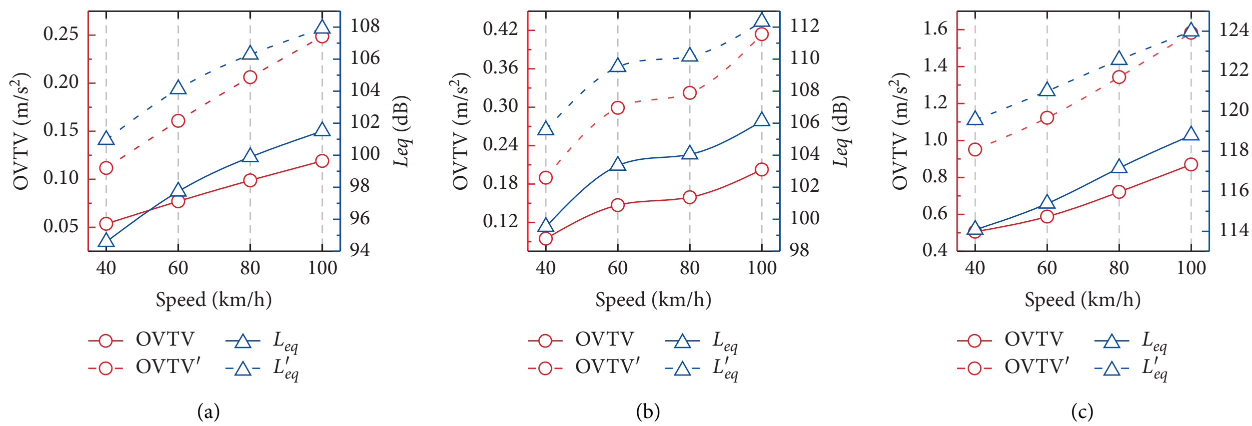

Figure 14: Comparison of comfort indices based on the traditional method and the new method under the influence of vehicle speed. (a) R0. (b) R1. (c) R2.

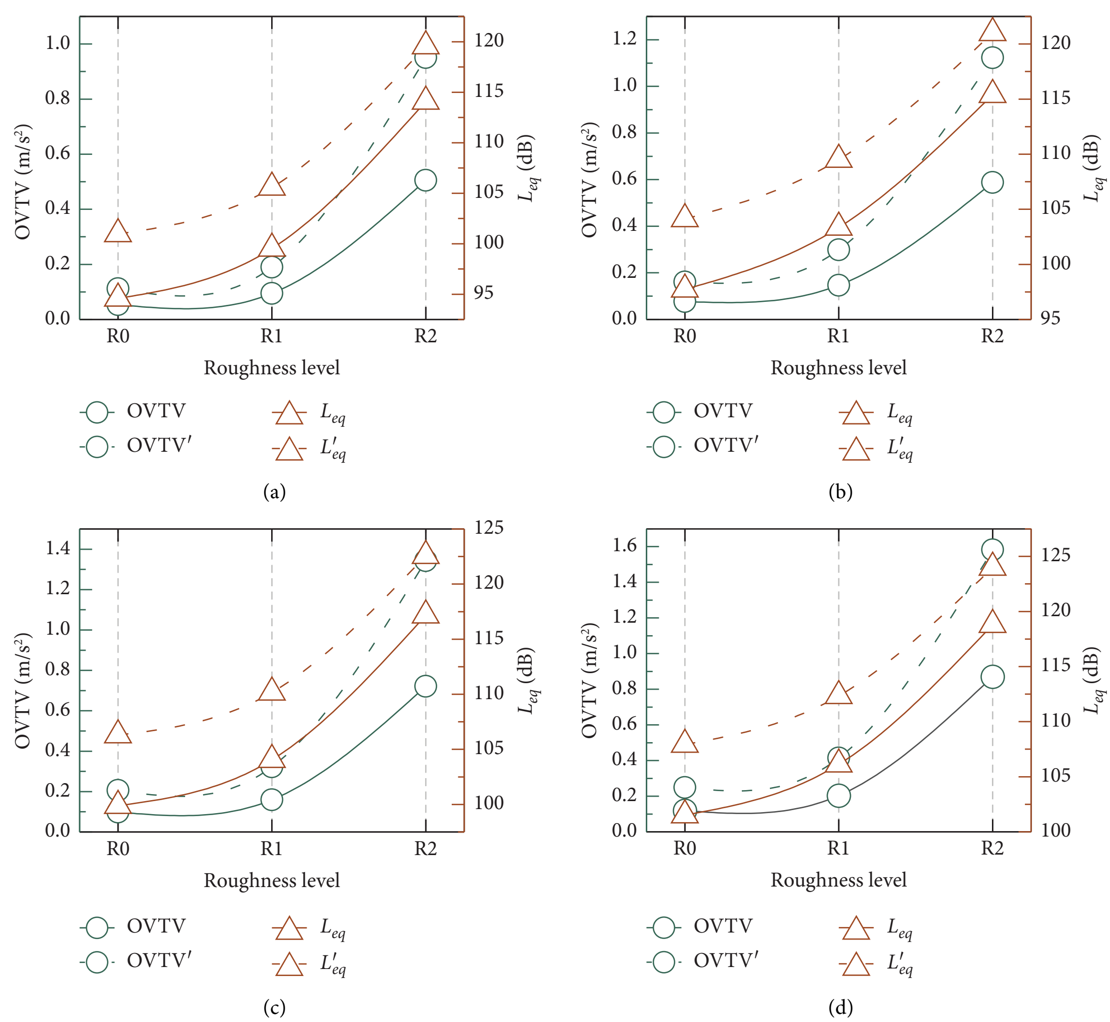

Figure 15: Comparison of comfort indices based on the traditional method and the new method under the influence of road surface roughness. (a) $V = 40$. (b) $V = 60$. (c) $V = 80$. (d) $V = 100$.

Table 7: Comfort index increase under the influence of vehicle speed.

Roughness level	Speed (km/h)	OVTV	OVTV′	Maximum increase (%)	L_{eq}	$L_{eq}^{'}$	Maximum increase (%)
R0	40	0.05	0.11	108.40	94.58	100.96	**6.74**
	60	0.08	0.16	108.79	97.73	104.12	6.54
	80	0.10	0.21	108.84	99.89	106.29	6.40
	100	0.12	0.25	**109.04**	101.51	107.91	6.31
R1	40	0.10	0.19	100.42	99.53	105.57	6.07
	60	0.15	0.30	103.35	103.35	109.51	**5.97**
	80	0.16	0.32	102.25	104.05	110.17	5.88
	100	0.20	0.41	**104.32**	106.14	112.34	5.85
R2	40	0.51	0.95	88.07	114.08	119.56	4.81
	60	0.59	1.12	**91.04**	115.39	121.01	**4.87**
	80	0.72	1.34	86.21	117.16	122.56	4.61
	100	0.87	1.58	81.93	118.79	123.99	4.38

The maximum values of these increases are shown in bold.

Table 8: Comfort index increase under the influence of bridge surface roughness.

Roughness level	Speed (km/h)	OVTV	OVTV′	Maximum increase (%)	L_{eq}	$L_{eq}^{'}$	Maximum increase (%)
40	R0	0.05	0.11	**108.40**	94.58	100.96	**6.74**
	R1	0.09	0.19	100.42	99.53	105.57	6.07
	R2	0.51	0.95	88.07	114.08	119.56	4.81
60	R0	0.08	0.16	**108.79**	97.73	104.12	**6.54**
	R1	0.15	0.30	103.35	103.35	109.51	5.97
	R2	0.59	1.12	91.04	115.39	121.01	4.87
80	R0	0.10	0.21	**108.84**	99.89	106.29	**6.40**
	R1	0.16	0.32	102.25	104.05	110.17	5.88
	R2	0.72	1.34	86.21	117.16	122.56	4.61
100	R0	0.12	0.25	**109.04**	101.51	107.91	**6.31**
	R1	0.20	0.41	104.32	106.14	112.34	5.85
	R2	0.87	1.58	81.93	118.79	123.99	4.38

The maximum values of these increases are shown in bold.

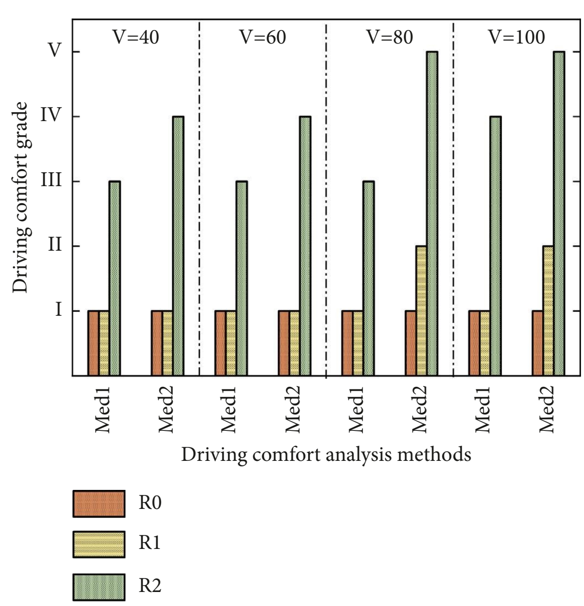

Figure 16: Comparison of driving comfort levels.

4. Conclusions

The paper introduces a new method for analyzing the driving comfort of highway bridges. This method comprehensively considers both the driver and vehicle vibrations and accounts for the roughness difference of wheel paths. By using a three-span continuous SCCBB as a case, the effectiveness and necessity of this method are compared and verified. The key findings are as follows:

(1) The HVBSI method directly captures the driver's vertical dynamic response, showing good agreement with the VBI method. The relative errors for peak values of VVD obtained through both methods consistently remain below 4%. Furthermore, the relative errors for the RMS values of VVA in the midpoint of the span are consistently below 9%. This affirms the reliability of employing the HVBSI method to address the vehicle-bridge interaction issue.

(2) Differences in wheel path roughness have minimal impact on vertical and pitch vibrations but significantly affect roll acceleration. Considering these roughness differences, RVA experiences a substantial increase of 12583.0%, with a significant rise in RMS value by 22839.22%. In contrast, the maximum increases in VVA and PVA are below 24%. Comfort indicators such as OVTV and L_{eq} show a noticeable increase, emphasizing the nonnegligible impact of wheel path roughness differences on driving comfort.

(3) Considering the driver's vertical vibration response, the driving comfort deteriorates compared to only considering the vehicle's dynamic response. Comfort indicators such as OVTV and L_{eq} show increased results compared to traditional methods, with maximum increments of 109.04% and 6.74%, respectively. This suggests that the traditional methods for bridge driving comfort evaluation may be somewhat conservative and highlight the necessity of comprehensively considering both the driver's body' dynamic response and the vehicle's dynamic response in driving comfort analysis.

(4) The mass-spring-damper-based elastic human body model lacks the ability to capture multidirectional vibrations directly. Current methods for simulating road surface roughness may underestimate the vehicle's roll vibration response. Further research is needed to develop comprehensive numerical simulation methods considering both the depth and width of road surface roughness, contributing to enhancing the highway bridge-driving comfort evaluation framework.

Data Availability

The data used to support the findings of the study are included within the article.

Conflicts of Interest

The authors declare that they have no conflicts of interest.

Acknowledgments

This research was funded by the National Key R&D Program of China (Grant nos. 2021YFB2600600 and 2021YFB2600605), the Key R&D Program of Hebei Province (Grant no. 19275405D), and the Postgraduate Innovation Fund Project of Hebei Province (Grant no. CXZZSS2023078).

References

[1] J. Zhao, *Study on Driving comfort of Long-Span cable-stayed Bridge Based on Bridge Deck Roughness*, Changsha University of Science & Technology, Changsha, China, 2014.

[2] S. S. Chen, S. Q. Ge, S. R. Gui, and H. Zhao, "Analysis on driving comfort of highway beam bridge based on vehicle-bridge coupling vibration," *Journal of East China Jiaotong University*, vol. 40, no. 1, pp. 1–9, 2023.

[3] G. C. Wang and W. S. Li, "Analysis on the vehicle ride comfort based on vehicle-bridge coupled vibration," *Journal of Vibration and Shock*, vol. 35, no. 8, pp. 224–230, 2016.

[4] J. Zhu, Z. Xiong, H. Xiang, X. Huang, and Y. Li, "Ride comfort evaluation of stochastic traffic flow crossing long-span suspension bridge experiencing vortex-induced vibration," *Journal of Wind Engineering and Industrial Aerodynamics*, vol. 219, Article ID 104794, 2021.

[5] Y. Han, J. Huang, C. S. Cai, and S. Chen, "Driving safety analysis of various types of vehicles on long-span bridges in crosswinds considering aerodynamic interference," *Wind and Structures*, vol. 4, no. 29, 2019.

[6] Y. Liu, X. Yin, L. Deng, and C. Cai, "Ride comfort of the bridge-traffic-wind coupled system considering bridge surface deterioration," *Wind and Structures*, vol. 23, no. 1, pp. 19–43, 2016.

[7] K. Nguyen, A. Camara, O. Rio, and L. Sparowitz, "Dynamic effects of turbulent crosswind on the serviceability state of vibrations of a slender arch bridge including wind-vehicle-bridge interaction," *Journal of Bridge Engineering*, vol. 22, no. 11, 2017.

[8] T. Wu, W. Qiu, G. Yao, and Z. W. Guo, "Vehicle ride comfort analysis on sea-crossing bridges under drift ice load," *Structures*, vol. 47, pp. 846–861, 2023.

[9] Q. Gao, K. Cui, Z. Li, and Y. Li, "Numerical investigation of the dynamic performance and riding comfort of a straddle-type monorail subjected to moving trains," *Applied Sciences*, vol. 10, no. 15, p. 5258, 2020.

[10] C. C. Liang, C. F. Chiang, and T. G. Nguyen, "Biodynamic responses of seated pregnant subjects exposed to vertical vibrations in driving conditions," *Vehicle System Dynamics*, vol. 45, no. 11, pp. 1017–1049, 2007.

[11] X. Xu, Z. R. Jing, Z. He, and Z. C. Zhang, "Calculation method for human-bridge vertically coupled vibration," *Journal of Vibration and Shock*, vol. 35, no. 5, 2016.

[12] S. Q. Wang, P. H. Peng, C. Yang, J. Ma, and T. Zhang, "Analysis of passenger-vehicle-bridge coupling vibration," *Journal of Vibration Engineering*, vol. 31, no. 1, pp. 30–38, 2018.

[13] G. Wang, J. Zhang, and X. Kong, "Study on passenger comfort based on human–bus–road coupled vibration," *Applied Sciences*, vol. 10, no. 9, p. 3254, 2020.

[14] S. Wang, M. Guo, X. Wang, H. Qiao, H. Xia, and Q. Ye, "Dynamic response and riding comfort analysis of a passenger-train-bridge system in urban rail transit," *International Journal of Structural Stability and Dynamics*, vol. 23, no. 6, 2023.

[15] S. Maeda, "Trend of International Standard ISO2631-1 (Evaluation of human exposure to whole-body vibration Vibration in buildings) and future tasks," *Journal of the Japan society of noise control engineering*, vol. 82, pp. 21–24, 2004.

[16] Y. Yu, L. Zhao, and C. Zhou, "A new vertical dynamic model for railway vehicle with passenger-train-track coupling vibration," *Proceedings of the Institution of Mechanical Engineers Part K: Journal of Multi-body Dynamics*, vol. 234, no. 1, pp. 134–146, 2020.

[17] X. J. Liu, X. Q. Zhang, and S. X. Zhang, "Vibration analysis and comfortableness evaluation of a human-vehicle-bridge coupled system," *Mechanical Science and Technology for Aerospace Engineering*, vol. 33, no. 9, pp. 1387–1392, 2014.

[18] X. M. Wang, *Structural Dynamic Analysis and Application with ANSYS*, China Communication Press, Beijing, China, 2014.

[19] S. C. Li, *Mechanical Vibration Road Surface Profiles Reporting of Mensured Data (GB/T7031-2005)*, China Machine Press, Beijing, China, 1995.

[20] J. Zhu, W. Zhang, and M. X. Wu, "Evaluation of ride comfort and driving safety for moving vehicles on slender coastal bridges," *Journal of Vibration and Acoustics*, vol. 140, no. 5, pp. 051012.1–051012.15, 2018.

[21] Y. F. Zhou and S. R. Chen, "Vehicle ride comfort analysis with whole-body vibration on long-span bridges subjected to crosswind," *Journal of Wind Engineering and Industrial Aerodynamics*, vol. 155, pp. 126–140, 2016.

[22] Y. Zhang, W. Li, Z. Ji, and G. Wang, "Vehicle ride comfort analysis based on vehicle-bridge coupled vibration," *Shock and Vibration*, vol. 2021, Article ID 5285494, 14 pages, 2021.

[23] M. J. Griffin, "Seating dynamics handbook of human vibration 9," *Handbook of Human Vibration*, pp. 387–414, Elsevier, Amsterdam, Netherlands, 1990.

[24] Z. B. Guo, J. Q. Bu, J. R. Zhang, W. L. Cao, and X. M. Huang, "Theoretical and numerical investigation of damage sensitivity of steel–concrete composite beam bridges," *Buildings*, vol. 13, no. 5, p. 1109, 2023.